ADVANCED FUNCTIONAL MATERIALS
www.afm-journal.de



# Electric-Field-Assisted Charge Generation and Separation Process in Transition Metal Oxide-Based Interconnectors for Tandem Organic Light-Emitting Diodes

*Jin-Peng Yang, Yan Xiao, Yan-Hong Deng, Steffen Duhm, Nobuo Ueno, Shuit-Tong Lee, Yan-Qing Li,* and Jian-Xin Tang**

**The charge generation and separation process in transition metal oxide (TMO)-based interconnectors for tandem organic light-emitting diodes (OLEDs) is explored using data on electrical and spectral emission properties, interface energetics, and capacitance characteristics. The TMO-based interconnector is composed of $MoO_3$ and cesium azide ($CsN_3$)-doped 4,7-diphenyl-1,10-phenanthroline (BPhen) layers, where $CsN_3$ is employed to replace the reactive metals as an n-dopant due to its air stability and low deposition temperature. Experimental evidences identify that spontaneous electron transfer occurs in a vacuum-deposited $MoO_3$ layer from various defect states to the conduction band via thermal diffusion. The external electric-field induces the charge separation through tunneling of generated electrons and holes from $MoO_3$ into the neighboring $CsN_3$-doped BPhen and hole-transporting layers, respectively. Moreover, the impacts of constituent materials on the functional effectiveness of TMO-based interconnectors and their influences on carrier recombination processes for light emission have also been addressed.**

## 1. Introduction

In recent years, tandem organic lighting emitting diodes (OLEDs) have been attracting more attention for the development of next-generation flat panel displays and solid-state lighting, because of their advantages with high brightness, long lifetime, and low energy consumption.[1–12] In tandem OLEDs, vertically stacked electroluminescent (EL) units are electrically linked in series by interconnectors, and the device characters such as brightness and current efficiency at a certain current density can scale linearly with the number of EL units.[1,2] Upon the application of an electric field, electrons and holes generated by the interconnectors will inject into the neighboring electron- and hole-transporting layers (ETL and HTL) of the individual EL units, and thereby recombine with holes injected from the anode side or electrons injected from the cathode side for light emission.[10–15] Therefore, the interconnectors that serve as the charge generation layer, are the critical factor for tandem OLEDs to function efficiently.[1–15] However, the mechanism of charge generation and separation within the interconnectors is not yet understood in a sufficient way.[10–19]

The interconnectors used in tandem OLEDs are typically a bilayer structure with various materials, including a metal–metal (or metal oxide) bilayer,[9] an organic–metal (or metal oxide) bilayer,[1,3–7] or an organic–organic bilayer.[2,10–12] In the interconnectors with an organic–metal oxide bilayer, transition metal oxides (TMOs) such as vanadium oxide ($V_2O_5$),[4,15] molybdenum trioxide ($MoO_3$),[5,16] and tungsten trioxide ($WO_3$),[7,9] are widely incorporated adjacent to the HTL of the neighboring EL unit due to their high work function and highly optical transparency in the visible region for photon output, while the organic layers adjacent to the ETL of another neighboring EL unit are commonly n-typed doped by alkaline metals or metal compounds (e.g., Li, Cs, $Cs_2CO_3$, etc).[2,5,13]

Parallel to various structures employed as the interconnectors in tandem OLEDs, several models have been proposed to interpret the charge carrier generation and separation process.[10–19] Kröger et al. proposed a temperature-independent tunneling-based charge generation model in doped organic–organic bilayer interconnectors via electric-field-induced electron transfer from the highest occupied molecular orbital (HOMO) of a p-type doped organic layer to the lowest unoccupied molecular orbital (LUMO) of an n-type doped organic layer,[14] which was supported by the energy level alignment obtained from the ultraviolet photoemission spectroscopy (UPS) measurements.[10,11] On the other hand, the mechanisms operating at TMO-organic

J.-P. Yang, Y. Xiao, Y.-H. Deng, Prof. Y.-Q. Li, Prof. J.-X. Tang
Jiangsu Key Laboratory for Carbon-Based Functional Materials & Devices
Institute of Functional Nano & Soft Materials (FUNSOM)
Soochow University
Suzhou 215123, P. R. China
E-mail: yqli@suda.edu.cn; jxtang@suda.edu.cn
Dr. S. Duhm, Prof. N. Ueno
Graduate School of Advanced Integration Science
Chiba University
1-33 Yayoi-cho, Inage-ku, Chiba 263-8522, Japan
Prof. S.-T. Lee
Center Of Super-Diamond and Advanced Films (COSDAF)
City University of Hong Kong
Hong Kong SAR, P. R. China

DOI: 10.1002/adfm.201102136

**Table 1.** Layer structures of the OLED devices.

| Devices or units | Layer structures |
|---|---|
| Device A | ITO/**EL**/LiF (0.5 nm)/Al (100 nm) |
| Device B | ITO/**EL**/$CsN_3$:BPhen (20 vol%, 20 nm)/$MoO_3$ (10 nm)/**EL**/LiF (0.5 nm)/Al (100 nm) |
| Device C | ITO/**EL**/$MoO_3$ (10 nm)/**EL**/LiF (0.5 nm)/Al (100 nm) |
| Device D | ITO/**EL**/$CsN_3$:BPhen (20 vol%, 20 nm)/**EL**/LiF (0.5 nm)/Al (100 nm) |
| Device E | ITO/**EL**/**EL**/LiF (0.5 nm)/Al (100 nm) |
| **EL** | NPB (40 nm)/C545T:$Alq_3$ (1 vol%, 20 nm)/BPhen (40 nm) |
| Device F | ITO/**EL-R**/$CsN_3$:BPhen (20 vol%, 20 nm)/$MoO_3$ (10 nm)/**EL-G**/LiF (0.5 nm)/Al (100 nm) |
| Device G | ITO/**EL-R**/$MoO_3$ (10 nm)/**EL-G**/LiF (0.5 nm)/Al (100 nm) |
| Device H | ITO/**EL-R**/$CsN_3$:BPhen (20 vol%, 20 nm)/**EL-G**/LiF (0.5 nm)/Al (100 nm) |
| Device I | ITO/**EL-R**/**EL-G**/LiF (0.5 nm)/Al (100 nm) |
| Device J | ITO/**EL-G**/$CsN_3$:BPhen (20 vol%, 20 nm)/$MoO_3$ (10 nm)/**EL-R**/LiF (0.5 nm)/Al (100 nm) |
| Device K | ITO/**EL-G**/$MoO_3$ (10 nm)/**EL-R**/LiF (0.5 nm)/Al (100 nm) |
| Device L | ITO/**EL-G**/$CsN_3$:BPhen (20 vol%, 20 nm)/**EL-R**/LiF (0.5 nm)/Al (100 nm) |
| Device M | ITO/**EL-G**/**EL-R**/LiF (0.5 nm)/Al (100 nm) |
| **EL-G** | NPB (40 nm)/$Alq_3$ (20 nm)/BPhen (40 nm) |
| **EL-R** | NPB (40 nm)/DCJTB:$Alq_3$ (3 vol%, 20 nm)/BPhen (40 nm) |

bilayer interconnectors remain a subject of debate.[15–19] Thermally assisted charge generation models have been proposed, in which TMOs were assumed to be p-type semiconductors and impurity levels above the valence band of TMOs were regarded as the sources of charge generation.[15,17] In contrast to the claim that electrons and holes were generated at TMO/ETL interfaces,[15,17] it has been supposed that charge generation and separation occur at the interface between TMOs and the adjacent HTL via electron transfer from the HTL's HOMO into the conduction band of TMOs.[12,16,18,19] Such understanding on TMO-organic bilayer interconnectors was primarily inferred from the electronic structures determined by UPS analysis, in which TMOs actually exhibit n-type semiconducting property with high work function and a deep-lying conduction band.[16,18–21] However, aside from various conjectures, direct evidence is yet lacking for clarifying which interface dominates the charge generation and separation process in TMO-based interconnectors, or whether the charge generation even occurs within the TMO layer.

To further understand the TMO-based interconnectors, we present a detailed study on charge generation and separation process in TMO-based interconnectors by systematically characterizing electrical and spectral emission properties, interface energetics, and capacitance–voltage characteristics through device fabrication, photoelectron spectroscopy, and impedance spectroscopy. The TMO-based interconnector is composed of a bilayer of $MoO_3$ and cesium azide ($CsN_3$)-doped 4,7-diphenyl-1,10-phenanthroline (BPhen). $CsN_3$ is employed to replace the typical reactive metals as an n-type dopant in the interconnector, because of its air stability and low deposition temperature demonstrated recently in tandem OLEDs.[22] The role of TMO and n-type doped organic layers in charge generation and separation, and their influence on the carrier recombination processes for light emission in tandem OLEDs have been identified.

## 2. Results and Discussion

### 2.1. Influence of Interconnectors on Device Characteristics

Tandem OLEDs were fabricated with two individual EL units, which were separated by different interconnectors, namely (1) $CsN_3$:BPhen/$MoO_3$, (2) $CsN_3$:BPhen, (3) $MoO_3$, and (4) none. The EL unit is composed of a hole-transporting layer (HTL) of *N*,*N*′-di(naphthalene-1-yl)-*N*,*N*′-diphenyl-benzidine (NPB), a green emitting layer of tris(8-hydroxyquinoline) aluminum ($Alq_3$) doped with 10-(2-benzothiazolyl)-2,3,6,7-tetrahydro-1,1,7,7-tetramethyl-1H,5H,11H-(1) benzopyropyrano(6,7,8-i,j)quinolizin-11-one (C545T), and an electron-transporting layer (ETL) of BPhen. The anode and cathode of the OLEDs are indium tin oxide (ITO) and LiF/Al bilayer, respectively. To minimize the effects due to different processing conditions, tandem devices with four different interconnectors were fabricated in the same lot by changing the shadow mask. For comparison, a reference device with a single EL unit was also prepared. The detailed layer structures of the devices are shown in **Table 1**.

**Figure 1** plots the current-density–voltage (*J*–*V*) characteristics and luminance efficiency of four tandem OLEDs (devices B–E) together with that of a reference OLED having only one EL unit (device A) for comparison. As observed in Figure 1a, the driving voltage of the tandem OLED with a $CsN_3$:Bphen/$MoO_3$ interconnector (device B) is almost twice compared to that of the reference device (device A) at a certain current density, which can be expected for a properly working tandem OLED. However, it is evident that the other tandem devices (devices C–E) exhibit a poor electrical property, and require a higher driving voltage compared to the device with the use of $CsN_3$:Bphen/$MoO_3$.

The luminance efficiency versus current density of devices C–E is comparable with that of the reference device A with a single EL unit (Figure 1b). The luminance efficiency of the tandem device B with the $CsN_3$:BPhen/$MoO_3$ interconnector is, however, almost twice than that of device A. For instance, at the current density of 20 mA $cm^{-2}$, the luminance efficiencies of tandem devices B–E and the reference single EL device A are 19.3, 13.7, 11.1, 6.8, and 10.1 cd $A^{-1}$, respectively. It is clearly noted that constituent materials of interconnectors are critical in their functional effectiveness and thus the carrier recombination processes for light emission in tandem OLEDs.

To gain a deeper understanding of the correlation between the carrier recombination processes and the difference in efficiency for tandem OLEDs with various interconnectors, two series of tandem devices combining green and red emission EL units (EL-G and EL-R) were further fabricated. For each series, four devices with different interconnectors were fabricated in the same lot by changing the shadow mask. The layer structures of these two series (i.e., devices F–I and J–M) are shown

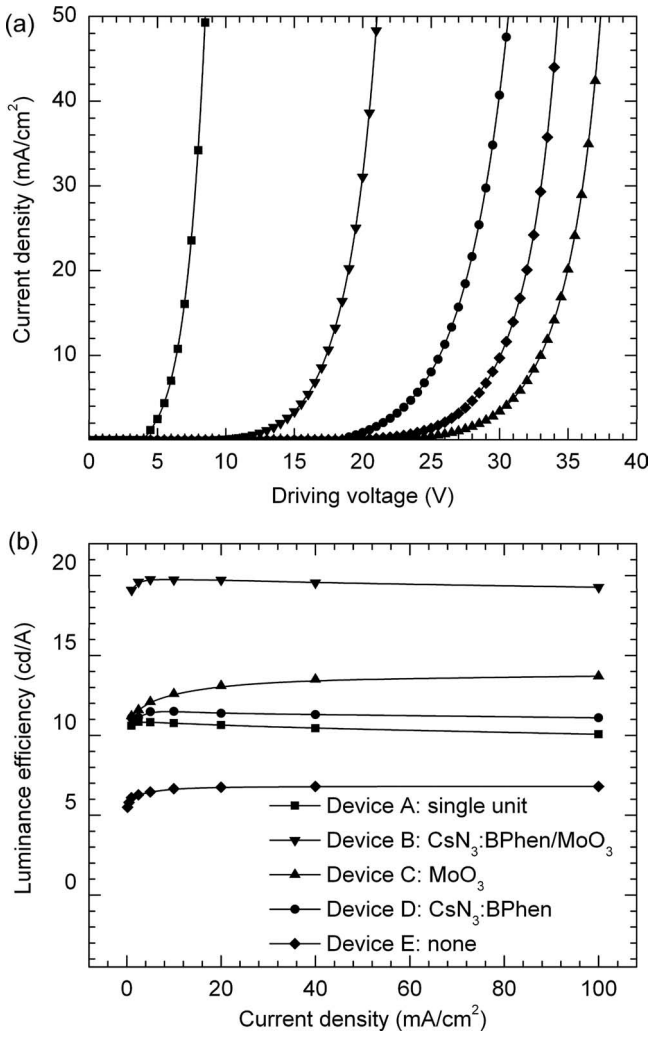


**Figure 1.** a) *J–V* and b) luminance efficiency-current density characteristics obtained from the single EL unit device A and tandem devices B–E with different interconnectors. The device configurations are shown in Table 1.

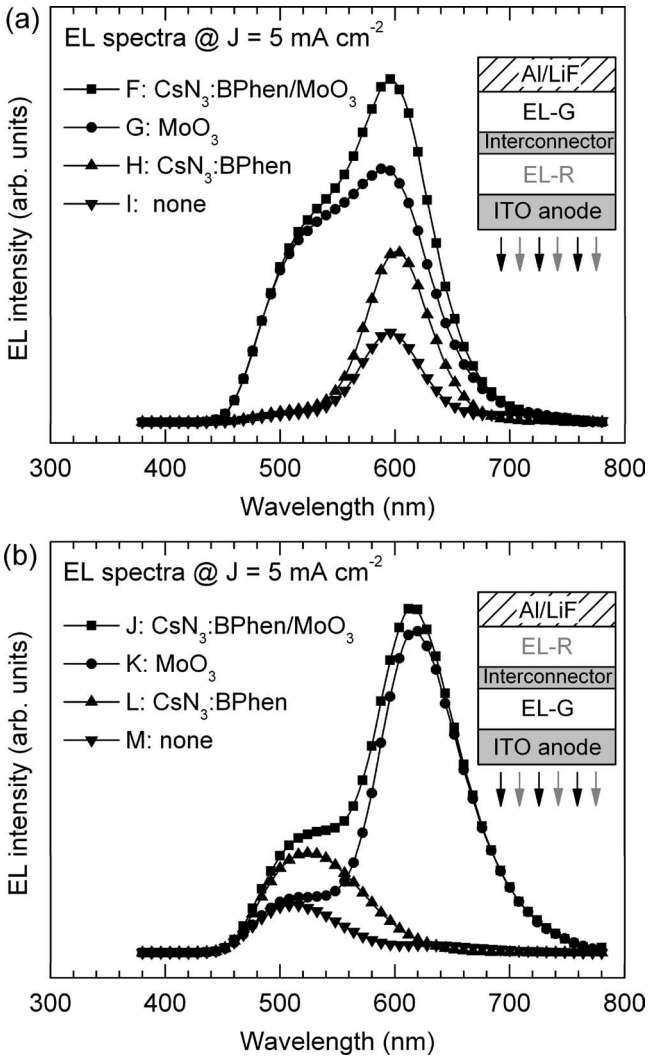


**Figure 2.** EL spectra of tandem devices with two different EL units. a) Devices F–I: the bottom EL unit having red emission and the top EL unit having green emission; b) devices J–M: the bottom EL unit having green emission and the top EL unit having red emission, respectively.

in Table 1. The EL-G comprises a NPB layer as the HTL, a BPhen layer as the ETL, and an $Alq_3$ layer as the green emission layer, while the EL-R is formed by a red emission layer of 4-(dicyanomethylene)-2-*t*-butyl-6-(1,1,7,7,-tetramethyl julolidyl-9-enyl)-4H-pyran (DCJTB)-doped $Alq_3$ located between the HTL of NPB and the ETL of BPhen. As depicted in the insets of **Figure 2**a and b, EL-G and EL-R in these two series are electrically connected by an interconnector in opposite sequence.

Figure 2 compares the EL spectra of two series of tandem devices at $J = 5$ mA cm$^{-2}$, in which the EL peaks with a wavelength of 520 nm corresponds to $Alq_3$ emission, while the EL peak at ~600 nm corresponds to DCJTB emission. As shown in Figure 2, EL spectra of tandem devices with various interconnectors help to identify the location of the emissive zones for these devices. With the use of the $CsN_3$:BPhen/$MoO_3$ interconnector in tandem OLEDs (devices F and J), both green and red emission components can be observed in Figures 2a and b, implying that such an interconnector functions well and emissions in both EL-G and EL-R units are mutually independent on the tandem structure. Similarly, both green and red emission features can be observed in EL spectra for tandem devices with only $MoO_3$ as the interconnector (devices G and K), except that the emission intensity from the EL unit at the anode side is relatively lower than that of devices F and J with a $CsN_3$:BPhen/$MoO_3$ interconnector. The emission behaviors of devices G and K indicate that the charge generation and hole injection into the HTL of the cathode side-EL unit are consistent with the tandem devices with a $CsN_3$:BPhen/$MoO_3$ interconnector, whereas the electron-hole recombination in the anode side-EL unit is prohibited due to the reduced electron injection into the neighboring ETL of BPhen without a $CsN_3$:BPhen layer. On the contrary, when only $CsN_3$:BPhen is used in the interconnector, the tandem devices (i.e., devices H and L) behave like an OLED with a single EL unit, where the emission from the EL unit at the anode side dominates the EL spectra with negligible emission from the cathode side-EL unit. For example, device H has

the emission of DCJTB from the EL-R unit and very little emission of $Alq_3$ from the EL-G unit, while device L exhibits the reverse behavior. Similar emission behaviors can be observed for tandem devices I and M without an interconnector between two EL units, while the emission intensities are rather lower than those of devices H and L, as shown in Figure 2a and b. The asymmetric contribution of two EL units to the EL spectra for devices H, I, L and M validates that the $MoO_3$ layer is essential to charge generation in the interconnector.

### 2.2. Interfacial Energetics on Interconnectors

To understand the origin of the difference in device performance and especially the impacts of constituent materials on the functional effectiveness of TMO-based interconnectors, the electronic structures of the interconnectors with the neighboring ETL and HTL layers were studied via ultraviolet and X-ray photoemission spectroscopy (UPS and XPS) measurements. **Figure 3**a shows the HeI UPS spectra of incremental $CsN_3$:BPhen deposition on a 100 Å-thick BPhen layer on the underlying ITO substrate. It is obvious that deposition of the $CsN_3$:BPhen overlayer on BPhen leads to an abrupt and rigid shift of energy levels towards higher binding energies (BEs). The shift of the secondary electron cutoff in the high BE region indicates a vacuum level (VL) shift of 1.1 eV, as shown in Figure 3a. The HOMO edges of $CsN_3$:BPhen and pristine BPhen can be extracted by the intercept of the tangent of the leading edges of the low BE feature and the background level, and are found at 4.4 and 3.3 eV below Fermi level ($E_F$), respectively. The ionization potential (IP) values, which were obtained by the energy difference between the HOMO edge and VL onset, are 6.4 eV for both $CsN_3$:BPhen and BPhen, respectively, and are thus in good agreement with previous data.[19]

In addition, two gap states with energy difference of 2.7 eV were formed in the energy gap of $CsN_3$:BPhen as shown in the inset of Figure 3a.[19] To accurately determine the chemical reactions at the BPhen/$CsN_3$:BPhen interface, XPS measurements were also taken after each deposition step. **Figure 4** displays the evolution of XPS spectra of C 1s, N 1s and Cs 3d5 core levels for the BPhen/$CsN_3$:BPhen interface. As evident in Figures 4a and b, C 1s and N 1s core levels exhibit an abrupt shift of ~1.2 eV towards higher BE with the appearance of a new feature at the low BE region upon the deposition of $CsN_3$:BPhen, which are consistent with the UPS results. As reported in the literature, $CsN_3$ was expected to have an n-doping effect through the decomposition into Cs and $N_2$ during the evaporation.[22] Therefore, the new peaks in C1s and N1s core level spectra represent chemical bonding among Cs, C and N in the $CsN_3$:BPhen layer.

The HeI UPS spectra of $MoO_3$ deposited onto $CsN_3$:BPhen layer are shown in Figure 3b, in which the bottom spectrum is identical to that of 100 Å-thick $CsN_3$:BPhen layer in Figure 3a. It is evident that deposition of the $MoO_3$ overlayer results in a progressive shift of emission features of $CsN_3$:BPhen and $MoO_3$ toward lower BEs, and the disappearance of the $CsN_3$:BPhen gap states, however, a $MoO_3$-derived gap state is emerging (vide infra). Similar to a previous report,[19] the Mo 3d core level spectra (not shown here) imply that a chemical reaction takes place at $CsN_3$:BPhen/$MoO_3$ interface, and some $CsN_3$-doped BPhen molecules are recovered to that of pristine

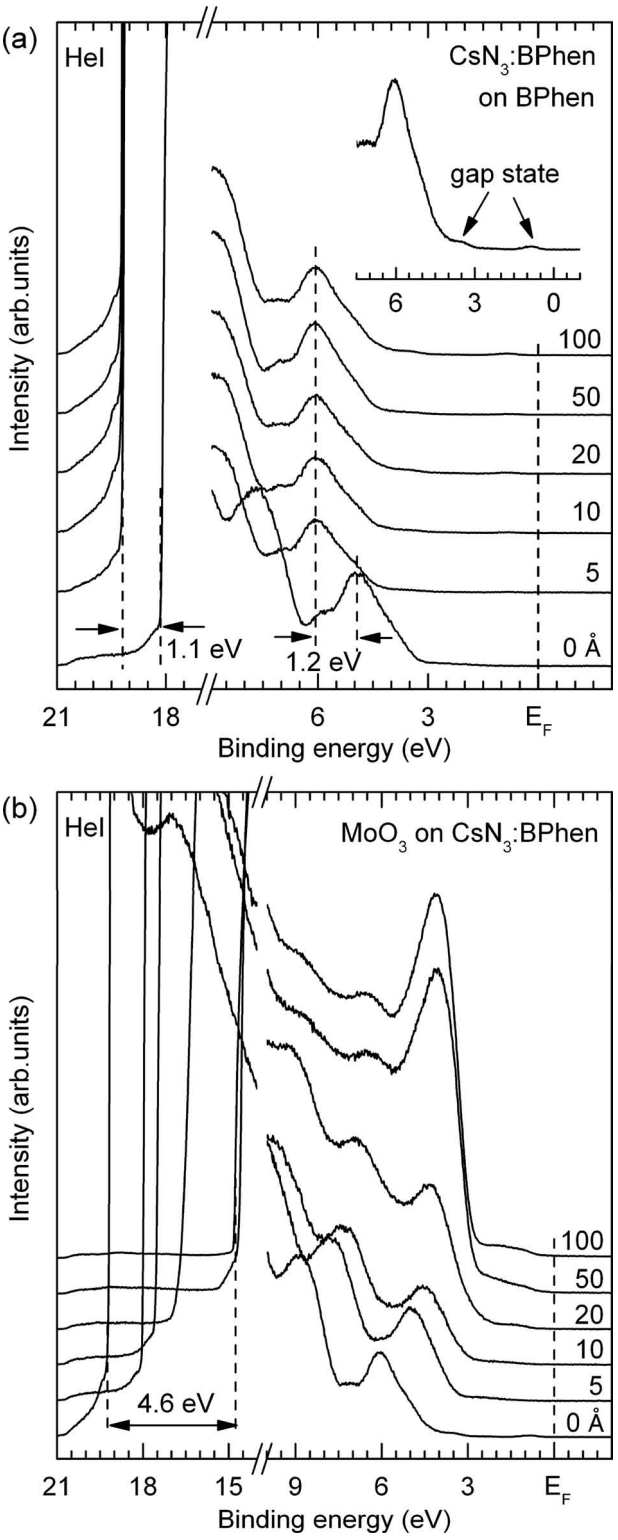


**Figure 3.** HeI UPS spectra of BPhen/$CsN_3$:BPhen (a) and $CsN_3$:BPhen/$MoO_3$ (b) interfaces as a function of incremental deposited layers. The inset shows the enlarged HOMO region of 100 Å-thick $CsN_3$:BPhen layer.

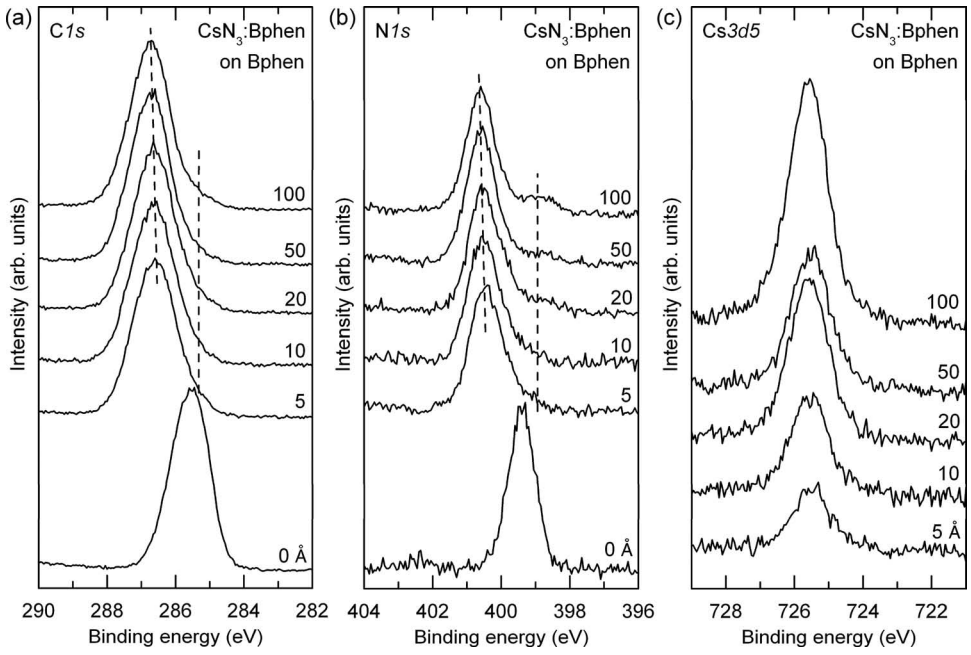


**Figure 4.** The evolution of (a) C 1s, (b) N 1s, and (c) Cs $3d_{5/2}$ core level XPS spectra upon the formation of the BPhen/$CsN_3$:BPhen interface. The dashed lines are added just for the guide for eyes.

BPhen via the reduction of $Mo^{6+}$ cations to $Mo^{5+}$ state. In contrast, the UPS spectral evolution of the BPhen/$MoO_3$ interface (not shown here) indicates the chemically inert nature without additional spectral structures upon $MoO_3$ deposition on BPhen layer. However, it is noted that the spectral features become saturated at 50 Å-thick $MoO_3$ layer, and are identical to that at the $CsN_3$:BPhen/$MoO_3$ interface.[19]

According to the top spectrum in Figure 3b, a 100 Å-thick $MoO_3$ layer possesses a high work function of 6.7 eV with the valence band maximum at 2.8 eV below $E_F$, which is consistent with previous reports.[19,20] Given that the energy gap of $MoO_3$ is around 3.1 eV,[20] the $MoO_3$ layer thus exhibits n-type semiconducting property with the conduction band minimum pinned slightly above $E_F$. In addition, it is obvious that deep-lying gap state emerges in the forbidden gap of $MoO_3$, which is related to the oxygen deficiency and partial reduction of $Mo^{6+}$ cation in accordance with XPS measurement in the literature.[19,20,23,24] The density of these gap states is so high that they not only dictate the position of the Fermi-level but may also act as a charge reservoir.

**Figure 5** displays the UPS spectra of a 100 Å-thick NPB layer incrementally deposited on $MoO_3$, BPhen, and $CsN_3$:BPhen substrates, respectively. No evidence of chemical reaction or formation of new interfacial electronic states can be observed for these three interfaces, which are in good agreement with previous data.[19,20,23,24] At the same time, these interfaces exhibit two different trends upon interface formation. The VL shift to higher BE side represents the formation of an interface dipole upon deposition of NPB on $MoO_3$, whereas the UPS spectra evolutions of $CsN_3$:BPhen/NPB and BPhen/NPB interfaces imply the absence of interface dipole at the corresponding interfaces.

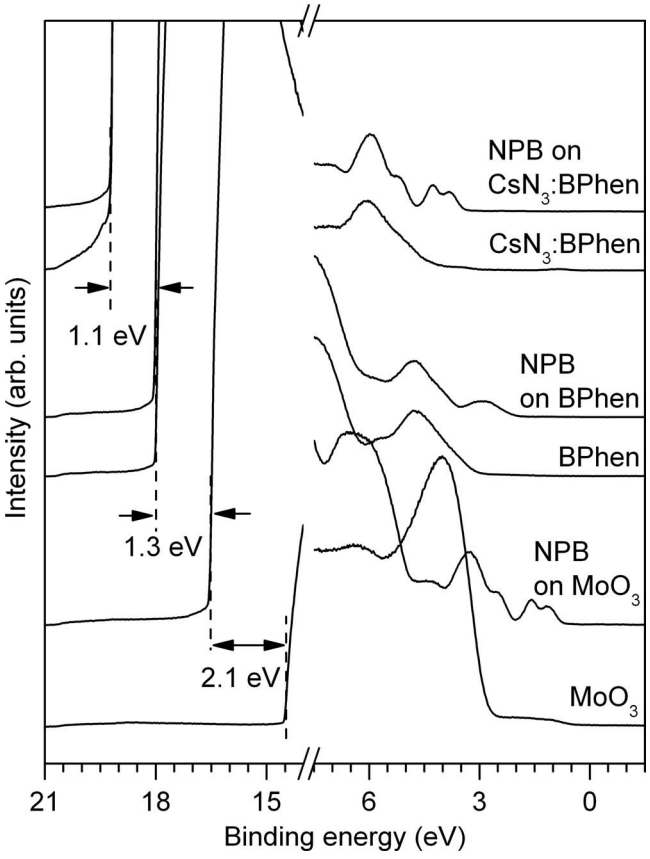


**Figure 5.** HeI UPS spectra of a 100 Å-thick NPB deposited on $MoO_3$, BPhen, and $CsN_3$:BPhen substrates, respectively.

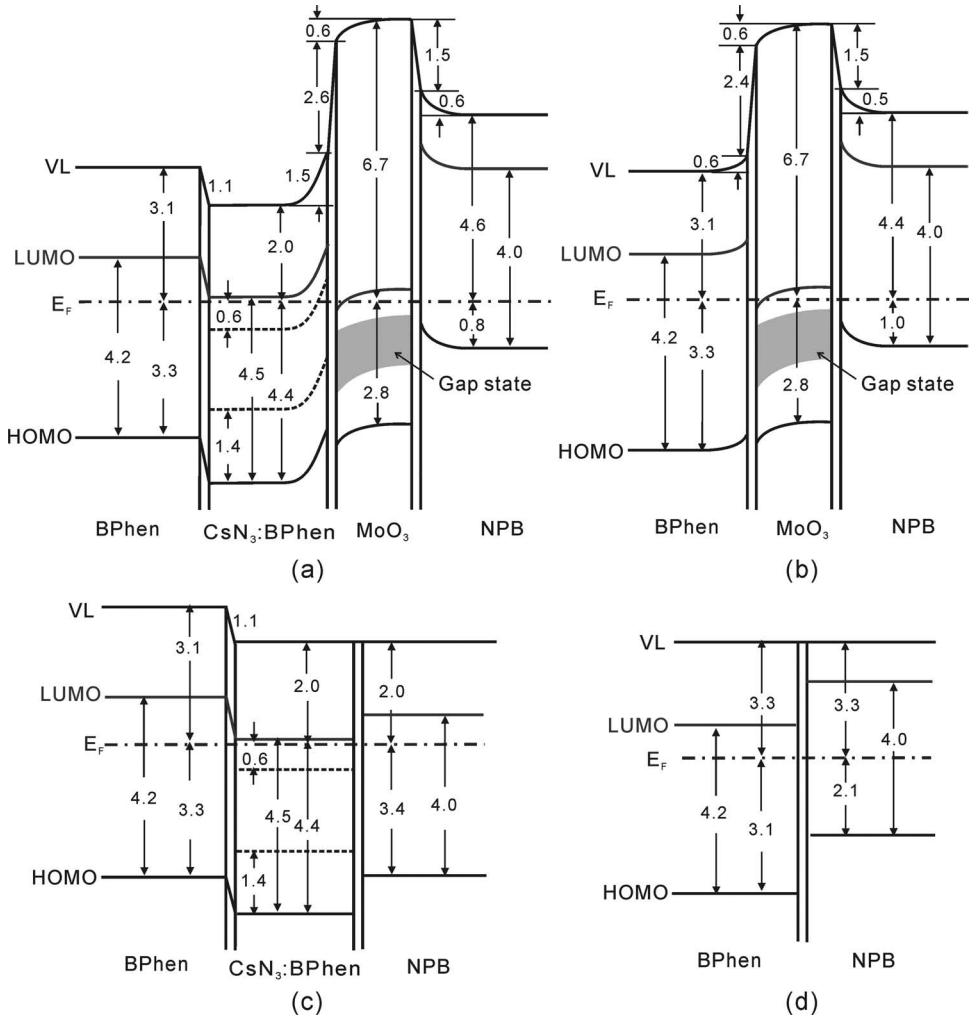


**Figure 6.** Schematic energy level diagrams: a) BPhen/$CsN_3$:BPhen/$MoO_3$/NPB, b) BPhen/$MoO_3$/NPB, c) BPhen/$CsN_3$:BPhen/NPB, and d) BPhen/NPB interfaces on ITO substrate, respectively. All the values shown are in the unit of eV.

**Figure 6** depicts the energy level diagrams for the discussed interconnectors obtained from UPS spectra: a) BPhen/$CsN_3$:BPhen/$MoO_3$/NPB, b) BPhen/$MoO_3$/NPB, c) BPhen/$CsN_3$:BPhen/NPB, and d) BPhen/NPB on ITO substrate, respectively. Here, HOMO (or valence band) positions are extracted from the UPS spectra, and LUMO (conduction band) positions are estimated by adding the charge-transport gaps (4.2 eV for BPhen, 4.5 eV for $CsN_3$:Bphen, 4.0 eV for NPB, and 3.1eV for $MoO_3$) relative to the HOMO energy levels.[16,19,20,23] $E_F$ of the underlying ITO substrate was used as energy reference, which was aligned across the interfaces in a thermodynamic equilibrium state. The contributions of interface dipole and energy level bending to the VL shift at the interfaces are taken into account in the energy level diagrams.

According to the energy level diagrams of the interconnectors with neighboring HTL and ETL layers depicted in Figure 6, the functional effectiveness of $MoO_3$-based interconnectors and thus the device performance of the corresponding tandem OLEDs shown in Figures 1 and 2 can be understood. As shown in Figure 6a and b, a p–n junction is formed between NPB and $MoO_3$ with a small hole injection barrier height. It has also been demonstrated that the hole-injection property of ambient contaminated $MoO_3$ surface is not significantly influenced, although the contamination reduces the work function of a low vacuum-grown $MoO_3$ film by about 1 eV with respect to the freshly evaporated film.[25–27] Therefore, it is expected that an electric-field-assisted charge generation and separation process can easily occur at the $MoO_3$/NPB interface via hole injection from $MoO_3$ into NPB's HOMO, as suggested previously.[13,23] However, the charge generation process could also happen within the TMO layer by exciting electrons from the oxygen vacancy derived gap states to the conduction band. The incorporation of a doped n-type organic layer in TMO-based interconnectors is also essential for tandem OLEDs to function efficiently with enhanced EL efficiency. As shown in Figure 6a and c, doping $CsN_3$ into BPhen can greatly move $E_F$ to only 0.1 eV below the LUMO, resulting in enhancing the electron injection and transport through $CsN_3$:BPhen into the BPhen ETL. Accordingly, electrons generated in $MoO_3$ can easily inject into $CsN_3$:BPhen's LUMO due to the small injection barrier at the

$CsN_3$:BPhen/$MoO_3$ interface. However, the large LUMO offset at the $MoO_3$/BPhen interface (see Figure 6b) limits the effective injection of electrons from $MoO_3$ into the BPhen layer of the ITO-side EL unit unless a higher driving voltage is added. Due to the insufficient electron injection and exciton formation, the resulting emission from the ITO-side EL unit is thus smaller than that of tandem OLED with a $CsN_3$:BPhen/$MoO_3$ interconnector.

Figures 6c and d show a typical flat vacuum level alignment at $CsN_3$:BPhen/NPB and BPhen/NPB interfaces, when $MoO_3$ was not involved in interconnectors. The large energy level offset between NPB's HOMO and $CsN_3$:BPhen's (or BPhen's) LUMO indicates that charge generation process is hard to occur at $CsN_3$:BPhen/NPB and BPhen/NPB interfaces unless a higher driving voltage is applied. In addition, the $CsN_3$:BPhen or BPhen layer could exhibit excellent hole-blocking capability for the emission layer of $Alq_3$ due to the wide bandgap and the large IP value. Therefore, the electron–hole recombination in the cathode-side EL unit for tandem OLEDs using interconnectors without $MoO_3$ is eliminated due to the lack of charge generation by $MoO_3$ and leakage current of holes from the ITO side. This is the reason why intensive emission from the cathode-side EL unit can only be observed for tandem OLEDs with $MoO_3$ in the interconnectors, while other tandem devices behave like an OLED with a single EL unit, as shown in Figure 2.

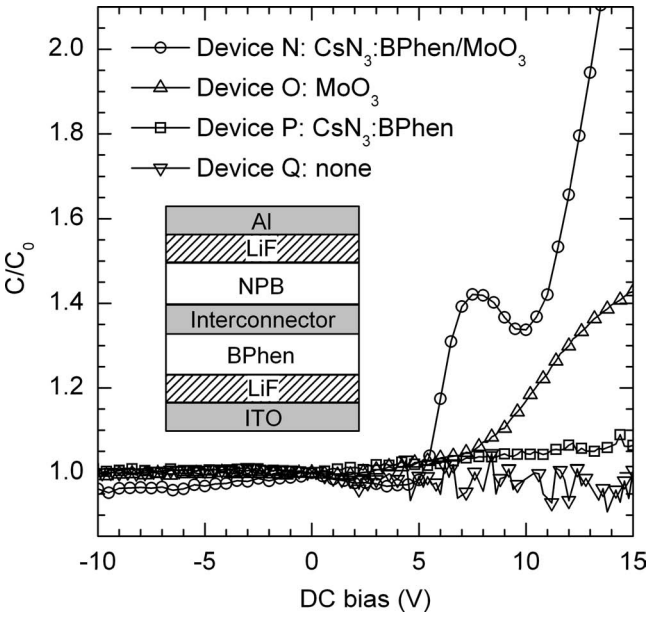


**Figure 7.** *C–V* characteristics of the interconnector device with a double-insulating structure measured at a fixed frequency of 1 kHz. $C_0$ is the zero bias value of capacitance. The inset shows the device structure.

### 2.3. Charge Generation Process in Interconnectors by Capacitance–Voltage Measurements

To further verify the electric field-assisted charge generation and separation process in TMO-based interconnectors, model devices were fabricated with a double-insulating structure of ITO/LiF/BPhen/Interconnector/NPB/LiF/Al (as shown in **Table 2**) and the corresponding capacitance-voltage (*C–V*) characteristics were measured under external electric fields. The forward bias in the *C–V* measurement was defined as the ITO electrode applied positively. The double-insulating layers of LiF were used to prohibit the charge injection from external electrodes, because it is usually difficult to be distinguished experimentally from the internal behaviors in the measured current flow.

**Figure 7** shows the capacitance of model devices with various interconnectors as a function of external DC bias at a fixed frequency of 1 kHz, where the measured capacitance (C) is normalized by the zero bias capacitance ($C_0$). It is observed that the capacitance for devices with $MoO_3$ in the interconnector (i.e., devices N and O) shows an abrupt increase when the forward bias exceeds a certain value, while no change in capacitance is observed under reverse bias. However, the capacitance of devices without $MoO_3$ (i.e., devices P and Q) is almost constant in the bias range, indicating neither displacement nor generation of charges within NPB and $CsN_3$:BPhen (or BPhen) layers. Therefore, the change in capacitance under forward bias is definitely associated with the presence of $MoO_3$ layer, where generated charges are transported through organic layers. These observations are consistent with the results in Figure 1 that no charge generation occurs in tandem OLEDs without $MoO_3$ in the interconnectors.

To identify the role of individual $Cs_2CO_3$:BPhen, $MoO_3$ and NPB layers in the change of capacitance, also *C–V* characteristics of devices R–U were examined at a fixed frequency of 1 kHz (see **Figure 8**). An increase of capacitance under forward bias can be observed in the case of device R, although the HTL

**Table 2.** Layer structures of double-insulating model devices for capacitance measurement.

| Devices | Layer structures |
|---|---|
| Device N | ITO/LiF (20 nm)/BPhen (40 nm)/$CsN_3$:BPhen (20 vol%, 20 nm)/$MoO_3$ (10 nm)/NPB (40 nm)/LiF (20 nm)/Al (100 nm) |
| Device O | ITO/LiF (20 nm)/BPhen (40 nm)/$MoO_3$ (10 nm)/NPB (40 nm)/LiF (20 nm)/Al (100 nm) |
| Device P | ITO/LiF (20 nm)/BPhen (40 nm)/$CsN_3$:BPhen (20 vol%, 20 nm)/NPB (40 nm)/LiF (20 nm)/Al (100 nm) |
| Device Q | ITO/LiF (20 nm)/BPhen (40 nm)/NPB (40 nm)/LiF (20 nm)/Al (100 nm) |
| Device R | ITO/LiF (20 nm)/BPhen (40 nm)/$CsN_3$:BPhen (20 vol%, 20 nm)/$MoO_3$ (10 nm)/LiF (20 nm)/Al (100 nm) |
| Device S | ITO/LiF (20 nm)/BPhen (40 nm)/$CsN_3$:BPhen (20 vol%, 20 nm)/$MoO_3$ (10 nm)/$CsN_3$:BPhen (20 vol%, 20 nm)/LiF (20 nm)/Al (100 nm) |
| Device T | ITO/LiF (20 nm)/NPB (40 nm)/$MoO_3$ (10 nm)/NPB (40 nm)/LiF (20 nm)/Al (100 nm) |
| Device U | ITO/LiF (20 nm)/BPhen (40 nm)/$MoO_3$ (10 nm)/BPhen (40 nm)/LiF (20 nm)/Al (100 nm) |

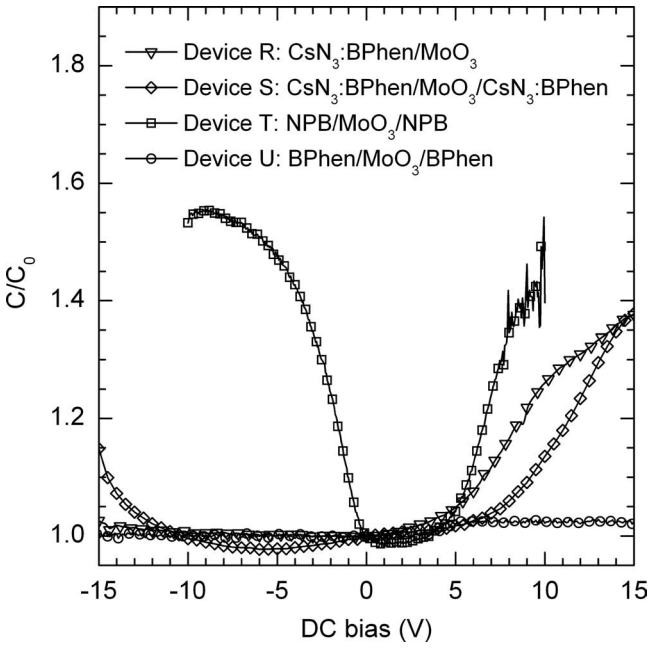


**Figure 8.** *C–V* characteristics of devices with a double-insulating structure at a fixed frequency of 1 kHz.

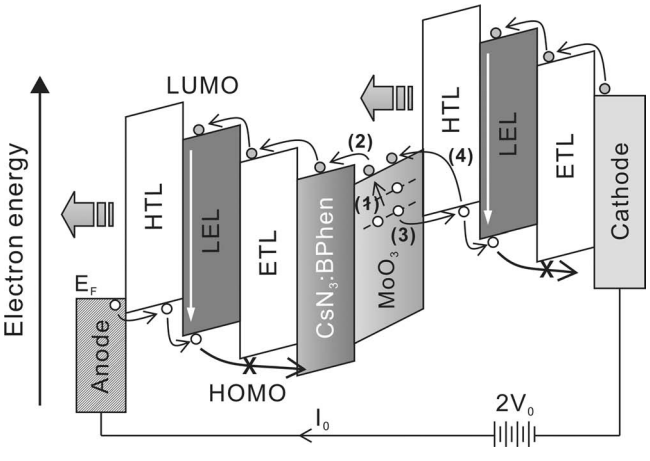


**Figure 9.** Schematic electric field-assisted charge generation and separation processes under forward bias: 1) electrons (solid circle) in deep-lying defect levels within $MoO_3$ are excited to the conduction band; 2) electrons are injected from $MoO_3$'s conduction band to the LUMO of $CsN_3$:BPhen layer; 3) holes (open circle) are injected from defect levels of $MoO_3$ to NPB's HOMO; 4) electrons are transferred directly from NPB's HOMO into $MoO_3$'s conduction band proposed previously.[13,16]

of NPB was removed as compared to device N in Figure 7. This result clearly indicates that the $MoO_3$/NPB interface is not the unique factor contributing to the charge generation process for TMO-based interconnector, which is contrary to the proposed mechanism reported in the literature.[13,16] Compared to device R, an additional $Cs_2CO_3$:BPhen layer was inserted between $MoO_3$ and LiF layers in device S, leading to capacitance changes under both forward and reverse biases. Similar behaviors were observed for device T with a $MoO_3$ layer between two NPB layers. On the contrary, no change in capacitance in the applied bias range was evident for device U, where the $MoO_3$ layer was sandwiched between two BPhen layers. This is due to the large energy offset between BPhen's LUMO and $MoO_3$'s conduction band as shown in Figure 6b, which is unfavorable to the electron injection from $MoO_3$ into the BPhen layer and thus limits the change in capacitance. These results definitely indicate that both $Cs_2CO_3$:BPhen/$MoO_3$ and $MoO_3$/NPB interfaces contribute to the charge separation process, although charges were generated within the $MoO_3$ layer. In addition, it can be understood that the non-monotonic dependence of capacitance on bias voltage for device N in Figure 7 is due to the presence of both $Cs_2CO_3$:BPhen/$MoO_3$ and $MoO_3$/NPB interfaces contributing to the charge displacement and therefore the increase in capacitance as compared to devices O and R.

**Figure 9** shows the schematic representation of charge generation and separation process in the $CsN_3$:BPhen/$MoO_3$ interconnector according the capacitance characteristics shown in Figures 7 and 8. Previously, the electric-field-assisted charge transfer was proposed to occur from occupied valence-band states of metal oxides to LUMO states of the n-type doped organic layer under applied bias.[4,15,17] However, as shown by Kröger et al.[23] and observed in Figure 3, $MoO_3$ exhibits n-type semiconducting property with a density of oxygen vacancies derived deep-lying defect states below $E_F$, which is observed in UPS and thus considerably high. Therefore, electron transfer in $MoO_3$ is expected to spontaneously occur via thermal diffusion from various defect states to the conduction band [denoted as process (1) in Figure 9]. Under forward bias, the electric field within $MoO_3$ layer induces tunneling of electrons and holes into the LUMO of $Cs_2CO_3$:BPhen and the HOMO of NPB [processes (2) and (3)], respectively. Then, electrons will immediately be driven away from $Cs_2CO_3$:BPhen to the BPhen layer by the external electric field, while holes are in the same way moved away from the interface. Such a displacement of charges at $Cs_2CO_3$:BPhen/$MoO_3$ and $MoO_3$/NPB interfaces gives rise to the capacitance changes, as shown in Figures 7 and 8. When the bias is inverted, no injection of electrons and holes occurs at $Cs_2CO_3$:BPhen/$MoO_3$ and $MoO_3$/NPB interfaces, exhibiting the unchanged capacitance. Although the proposed charge generation and separation process [processes (1–3) in Figure 9] is different from the mechanisms reported previously,[13,16] in which electrons were transferred from the NPB's HOMO to the TMO's conduction band, and then moved to the n-type doped organic layer [processes (4) and (2)], our experimental results do not exclude that such a process happens additionally. However, it is important for further device design to take in mind that the high density of intrinsic $MoO_3$ gap states closes the gap of 3.1 eV to a few hundred meV and thus leads to the concomitant n- and p-type behavior of $MoO_3$. The density of the $MoO_3$ oxygen vacancies derived gap states can be increased by vacuum-annealing,[20] and even more importantly for actual devices, also prevails for ex situ processed $MoO_3$.[25]

## 3. Conclusions

In summary, the functionality of TMO-based interconnectors for tandem OLEDs is demonstrated by systematically

investigating electrical and spectral emission properties, interface energetics, and capacitance characteristics. These findings show that vacuum-deposited $MoO_3$ layer acts as a charge generation layer due to spontaneous electron transfer from various defect states to the conduction band via thermal diffusion. The external electric-field induces the charge separation via injection of electrons and holes into the neighboring $CsN_3$-doped BPhen and hole-transporting layers, respectively. Moreover, the $CsN_3$-doped BPhen layer not only facilitates the electron extraction into the neighboring ETL, but also blocks the leakage of holes across the interconnector into the HTL of the adjacent EL unit.

## 4. Experimental Section

*Device Fabrication and Characterization*: All the devices were fabricated on patterned indium tin oxide (ITO)-coated glass substrates with a sheet resistance of 30 Ω $sq^{-1}$. Prior to film deposition, the ITO glass substrates were subjected to a routine cleaning process, and finally treated by UV-ozone exposure. All the organic and inorganic layers were thermally deposited within a high vacuum deposition system at a base pressure of $2 \times 10^{-6}$ Torr through a shadow mask. Deposition rates of different layers were monitored with quartz-crystal monitors and controlled to be 1–2 Å $s^{-1}$. The doping of organic layers was performed by thermal co-evaporation from individual sources, which are controlled via two quartz-crystal monitors. The current density-voltage-luminance (*J–V–L*) characteristics and EL spectra of the corresponding devices were measured simultaneously with a programmable Keithley model 2400 power source and a PhotoResearch PR 655 spectrometer in air ambience at room temperature.

*Interfacial Electronic Structure Characterization*: The ultraviolet and X-ray photoemission spectroscopy (UPS and XPS) characterization were conducted in a Kratos AXIS $Ultra^{DLD}$ ultrahigh-vacuum (UHV) surface analysis system, consisting of a multiport carousel chamber (base pressure $<5 \times 10^{-10}$ Torr), a deposition chamber ($<5 \times 10^{-10}$ Torr), and an analysis chamber ($<3 \times 10^{-10}$ Torr). The ITO substrates were ex situ solvent cleaned and UV-ozone treated. Thin films were in situ evaporated in steps onto substrates in the deposition chamber at growth rates of 1–2 Å $s^{-1}$. Prior to deposition, all materials were entirely outgassed to ensure material purity. After each deposition step, samples were directly transferred to the analysis chamber without breaking high vacuum for UPS and XPS measurements. UPS analysis was performed to characterize the valence states and the vacuum level (VL) with an unfiltered He I (21.2 eV) gas discharge lamp and a total instrumental energy resolution of 100 meV. Samples were negatively biased for the collection of secondary electrons. XPS measurements using a monochromatic Al Kαsource (1486.6 eV) were conducted to study the interfacial chemical reactions and the development of energy level bending with a resolution of 0.5 eV. All measurements were performed at room temperature.

*Capacitance Measurements*: Capacitance–voltage (*C–V*) measurements were performed using a Keithley 4200-CVU Semiconductor Characterization System with the samples stored in a high vacuum (~$10^{-6}$ Torr) probe station. A 50 mV amplitude AC signal superimposed on a DC bias was used to measure device capacitance as a function of AC frequency and DC bias under vacuum. In all *C–V* measurements, positive voltage (forward bias) was defined as the ITO electrode applied positively.

## Acknowledgements

The authors acknowledge the financial support by the National Natural Science Foundation of China (No. 61107022, 91027041, 61007020, 61036009, 60937001), National Basic Research Program of China (973 program) (No. 2010CB934502), the Research Fund for the Doctoral Program of Higher Education of China (No. 20093201120019, 20103201120019), the Natural Science Foundation of Jiangsu Province (No. BK2011280), and a Project Funded by the Priority Academic Program Development of Jiangsu Higher Education Institutions (PAPD). N.U. and S.D. acknowledge the Global-COE Program of MEXT (G03: Advanced School for Organic Electronics, Chiba University) and Grant-in-Aid for Scientific Research (A) (20245039).

Received: September 8, 2011
Published online: November 29, 2011

[1] T. Chiba, Y. J. Pu, R. Miyazaki, K. I. Nakayama, H. Sasabe, J. Kido, *Org. Electron.* **2011**, *12*, 710.
[2] L. S. Liao, W. K. Slusarek, T. K. Hatwar, M. L. Ricks, D. L. Comfort, *Adv. Mater.* **2008**, *20*, 324.
[3] C. W. Chen, Y. J. Lu, C. C. Wu, E. H. E. Wu, C. W. Chu, Y. Yang, *Appl. Phys. Lett.* **2005**, *87*, 241121.
[4] T. Tsutsui, M. Terai, *Appl. Phys. Lett.* **2004**, *84*, 440.
[5] H. Kanno, R. J. Holmes, Y. Sun, S. K. Cohen, S. R. Forrest, *Adv. Mater.* **2006**, *18*, 339.
[6] P. Chen, Q. Xue, W. F. Xie, G. H. Xie, Y. Duan, Y. Zhao, S. Y. Liu, L. Y. Zhang, B. Li, *Appl. Phys. Lett.* **2009**, *95*, 123307.
[7] C. C. Chang, S. W. Hwang, C. H. Chen, J. F. Chen, *Jpn. J. Appl. Phys., Part 1* **2004**, *43*, 6418.
[8] J. Drechsel, B. Mannig, D. Gebeyehu, M. Pfeiffer, K. Leo, H. Hoppe, *Org. Electron.* **2004**, *5*, 175.
[9] H. M. Zhang, Y. F. Dai, D. G. Ma, H. M. Zhang, *Appl. Phys. Lett.* **2007**, *91*, 123504.
[10] M. K. Fung, K. M. Lau, S. L. Lai, C. W. Law, M. Y. Chan, C. S. Lee, S. T. Lee, *J. Appl. Phys.* **2008**, *104*, 034509.
[11] J. X. Tang, M. K. Fung, C. S. Lee, S. T. Lee, *J. Mater. Chem.* **2010**, *20*, 2539.
[12] Y. M. Cheng, H. H. Lu, T. H. Jen, S. A. Chen, *J. Phys. Chem. C* **2011**, *115*, 582.
[13] S. Hamwi, J. Meyer, M. Kröger, T. Winkler, M. Witte, T. Riedl, A. Kahn, W. Kowalsky, *Adv. Funct. Mater.* **2010**, *20*, 1762.
[14] M. Kröger, S. Hamwi, J. Meyer, T. Dobbertin, T. Riedl, W. Kowalsky, H.-H. Johannes, *Phys. Rev. B* **2007**, *75*, 235321.
[15] M. Terai, K. Fujita, T. Tsutsui, *Jpn. J. Appl. Phys., Part 2* **2005**, *44*, L1059.
[16] J. Meyer, M. Kröger, S. Hamwi, F. Gnam, T. Riedl, W. Kowalsky, A. Kahn, *App. Phys. Lett.* **2010**, *96*, 193302.
[17] X. Qi, N. Li, S. R. Forrest, *J. Appl. Phys.* **2010**, *107*, 014514.
[18] Q. Y. Bao, J. P. Yang, J. X. Tang, Y. Q. Li, C. S. Lee, S. T. Lee, *Org. Electron.* **2010**, *11*, 1578.
[19] Q. Y. Bao, J. P. Yang, Y. Q. Li, J. X. Tang, *Appl. Phys. Lett.* **2010**, *97*, 063303.
[20] K. Kanai, K. Koizumi, S. Ouchi, Y. Tsukamoto, K. Sakanoue, Y. Ouchi, K. Seki, *Org. Electron.* **2010**, *11*, 188.
[21] D. Y. Kim, J. Subbiah, G. Sarasqueta, F. So, H. Ding, Irfan, Y. Gao, *Appl. Phys. Lett.* **2009**, *95*, 093304.
[22] K. S. Yook, S. O. Jeon, S. Y. Min, J. Y. Lee, H. J. Yang, T. Noh, S. K. Kang, T. W. Lee, *Adv. Funct. Mater.* **2010**, *20*, 1797.
[23] M. Kröger, S. Hamwi, J. Meyer, T. Riedl, W. Kowalsky, A. Kahn, *Appl. Phys. Lett.* **2009**, *95*, 123301.
[24] C. T. Lin, C. H. Yeh, M. H. Chen, S. H. Hsu, T. W. Pi, *J. Appl. Phys.* **2010**, *107*, 053703.
[25] J. Meyer, A. Shu, M. Kröger, A. Kahn, *Appl. Phys. Lett.* **2010**, *96*, 133308.
[26] J. Meyer, S. Hamwi, T. Bülow, H.-H. Johannes, T. Riedl, W. Kowalsky, *Appl. Phys. Lett.* **2007**, *91*, 113506.
[27] Irfan, H. Ding, Y. Gao, C. Small, D. Y. Kim, J. Subbiah, F. So, *Appl. Phys. Lett.* **2010**, *96*, 243307.